

# Supplementary Material for ‘Building blocks that govern spontaneous and programmed pattern formation in pre-compressed bilayers’

Jiajia Shen, Alberto Pirrera, Rainer M. J. Groh

## 1 Finite element formulation for pre-compressed bilayers and generalised path-following technique

### 1.1 Weak form of the equilibrium statement and linearisation

The principle of virtual work written in a total Lagrangian framework is

$$\int_{0V} {}^{t+\Delta t} S_{ij} \delta {}^{t+\Delta t} E_{ij} d^0V = {}^{t+\Delta t} R \quad (1)$$

where  $S_{ij}$  are Cartesian components of the second Piola-Kirchhoff stress tensor,  $E_{ij}$  are Cartesian components of the Green-Lagrange strain tensor, and  $R$  is the external virtual work; sub- and superscripts 0 and  $t + \Delta t$  represent the initial reference state and predicted state at  $t + \Delta t$ , respectively. The state at  $t + \Delta t$  can be written in terms of the state at  $t$  and an incremental term:  ${}^{t+\Delta t} S_{ij} = {}^t S_{ij} + {}_0 S_{ij}$  and  ${}^{t+\Delta t} E_{ij} = {}^t E_{ij} + {}_0 E_{ij}$ . The incremental strain tensor can be decomposed into linear and nonlinear parts as

$${}_0 E_{ij} = {}_0 e_{ij} + {}_0 \eta_{ij}, \quad (2)$$

where  ${}_0 e_{ij} = ({}_0 u_{i,j} + {}_0 u_{j,i} + {}^t u_{k,i} {}_0 u_{k,j} + {}_0 u_{k,i} {}^t u_{k,j})/2$  and  ${}_0 \eta_{ij} = {}_0 u_{k,i} {}_0 u_{k,j}/2$  are linear and quadratic in the incremental displacement components  ${}_0 u_i$ , respectively, with repeated indices  $k$  denoting summation and subscripted commas denoting partial differentiation. Note that the variation  $\delta {}^{t+\Delta t} E_{ij} = \delta {}_0 E_{ij}$ , such that Eq. (1) can be written as

$$\int_{0V} {}_0 S_{ij} \delta {}_0 E_{ij} d^0V + \int_{0V} {}^t S_{ij} \delta {}_0 \eta_{ij} d^0V = {}^{t+\Delta t} R - \int_{0V} {}^t S_{ij} \delta {}_0 e_{ij} d^0V. \quad (3)$$

For both linear and nonlinear elastic constitutive behaviour the incremental stress is linearly proportional to the strain increment via the instantaneous elasticity tensor  ${}_0 D_{ijkl}$ , *i.e.*  ${}_0 S_{ij} = {}_0 D_{ijkl} {}_0 E_{kl}$ . By neglecting terms that are more than quadratic in  ${}_0 u_i$ , Eq. (3) can be linearised as

$$\int_{0V} {}_0 D_{ijkl} {}_0 e_{kl} \delta {}_0 e_{ij} d^0V + \int_{0V} {}^t S_{ij} \delta {}_0 \eta_{ij} d^0V = {}^{t+\Delta t} R - \int_{0V} {}^t S_{ij} \delta {}_0 e_{ij} d^0V. \quad (4)$$

### 1.2 Constitutive modelling with thermal pre-strain

Both film and substrate are modelled using a compressible Neo-Hookean hyperelastic material model [1]. Note that a ‘nearly’ incompressible Neo-Hookean material (with incompressibility enforced using a penalty constraint [1]) was also implemented, with minor quantitative and no qualitative changes to the bifurcation manifolds. The Neo-Hookean material features parameters that are recognised from a familiar linear elastic material model. The Helmholtz free energy of the compressible Neo-Hookean material is given by

$$\Phi = \frac{\mu}{2} (I_C - 3) - \mu \ln J + \frac{\lambda}{2} (\ln J)^2, \quad (5)$$

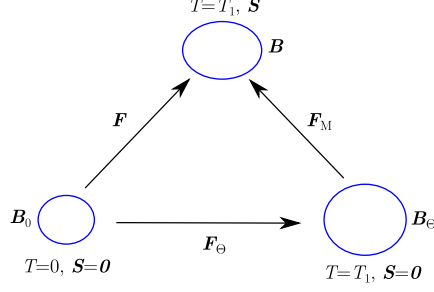


Figure 1: Decomposition of the deformation gradient tensor into a thermally-induced part ( $\mathbf{F}_\Theta$ ) and an elastic part ( $\mathbf{F}_M$ ).  $\mathbf{B}_0$ ,  $\mathbf{B}_\Theta$  and  $\mathbf{B}$  represent the reference state, intermediate state and current state respectively.

where  $I_C = \text{tr}\mathbf{C}$  and  $J^2 = \det\mathbf{C}$  with  $\mathbf{C} = \mathbf{F}^\top \mathbf{F}$  being the right Cauchy-Green deformation tensor derived from the deformation gradient tensor  $\mathbf{F}$ . Lamé's first parameter is given by  $\lambda = E\nu/[(1+\nu)(1-2\nu)]$  and the shear modulus is expressed as  $\mu = E/[2(1+\nu)]$  with  $E$  and  $\nu$  representing the Young's modulus and Poisson's ratio, respectively. Note that when there is no deformation, *i.e.*  $\mathbf{C} = \mathbf{I}$ , the stored energy function vanishes as expected.

The second Piola-Kirchhoff stress tensor  $\mathbf{S}$  is obtained by differentiation of Eq. (5) with respect to  $\mathbf{C}$ :

$$\mathbf{S} = 2 \frac{\partial \Phi}{\partial \mathbf{C}} = \mu(\mathbf{I} - \mathbf{C}^{-1}) + \lambda(\ln J)\mathbf{C}^{-1}. \quad (6)$$

Further, the Lagrangian elasticity tensor is obtained by differentiation of Eq. (6) with respect to  $\mathbf{C}$ :

$$\mathbb{D} = 2 \frac{\partial \mathbf{S}}{\partial \mathbf{C}} = \lambda \mathbf{C}^{-1} \otimes \mathbf{C}^{-1} + 2(\mu - \lambda \ln J)(\mathbf{C}^{-1} \odot \mathbf{C}^{-1}), \quad (7)$$

where  $(\mathbf{C}^{-1} \otimes \mathbf{C}^{-1})_{ABCD} = \mathbf{C}_{AB}^{-1} \mathbf{C}_{CD}^{-1}$  and  $(\mathbf{C}^{-1} \odot \mathbf{C}^{-1})_{ABCD} = (\mathbf{C}_{AC}^{-1} \mathbf{C}_{BD}^{-1} + \mathbf{C}_{AD}^{-1} \mathbf{C}_{BC}^{-1})/2$ .

For plane strain problems, the right Cauchy-Green deformation tensor  $\mathbf{C}$  can be obtained explicitly from the in-plane displacement gradient

$$\mathbf{C} = \mathbf{F}^\top \mathbf{F} = \begin{bmatrix} 1 + \frac{\partial u_1}{\partial x_1} & \frac{\partial u_1}{\partial x_2} \\ \frac{\partial u_2}{\partial x_1} & 1 + \frac{\partial u_2}{\partial x_2} \end{bmatrix}^\top \begin{bmatrix} 1 + \frac{\partial u_1}{\partial x_1} & \frac{\partial u_1}{\partial x_2} \\ \frac{\partial u_2}{\partial x_1} & 1 + \frac{\partial u_2}{\partial x_2} \end{bmatrix}. \quad (8)$$

The stress tensor  $\mathbf{S}$  and the elasticity tensor  $\mathbb{D}$  can be determined by substituting the in-plane right Cauchy-Green tensor from Eq. (8) in to Eqs. (6) and (7), respectively. For plane strain problems, the elasticity tensor  $\mathbb{D}$  can be written as:

$$\mathbb{D} = \begin{bmatrix} D_{1111} & D_{1122} & D_{1112} \\ D_{1122} & D_{2222} & D_{1222} \\ D_{1112} & D_{1222} & D_{1212} \end{bmatrix}. \quad (9)$$

Pre-strain in the substrate is modelled using a multiplicative decomposition of the deformation gradient tensor  $\mathbf{F}$ . This decomposition represents a stress-free expansion/contraction of the substrate into an intermediate state (*e.g.* through growth, swelling, or thermal expansion) followed by additional elastic and stress-inducing deformation that ensures compatibility with the attached film, see 1.3. In this paper, a thermal representation of the multiplicative decomposition is chosen for convenience. Hence, an intermediate configuration  $\mathbf{B}_\Theta$  is introduced by de-stressing the current material configuration  $\mathbf{B}$ , see Figure 1. If we set the elastic deformation gradient from  $\mathbf{B}_\Theta$  to  $\mathbf{B}$  to be  $\mathbf{F}_M$  and the thermal deformation gradient from  $\mathbf{B}_0$  to  $\mathbf{B}_\Theta$  as  $\mathbf{F}_\Theta$ , the total deformation gradient  $\mathbf{F} = \partial \mathbf{X} / \partial \mathbf{X}_0$  can be written as  $\mathbf{F} = \mathbf{F}_M \mathbf{F}_\Theta$ , where  $\mathbf{F}_M = \partial \mathbf{X} / \partial \mathbf{X}_\Theta$  and  $\mathbf{F}_\Theta = \partial \mathbf{X}_\Theta / \partial \mathbf{X}_0$ .

The Green-Lagrange strain tensor can then be written as

$$\mathbf{E} = \frac{1}{2}(\mathbf{F}^\top \mathbf{F} - \mathbf{I}) = \frac{1}{2}(\mathbf{C} - \mathbf{I}) = \mathbf{E}_\Theta + \mathbf{F}_\Theta^\top \mathbf{E}_M \mathbf{F}_\Theta, \quad (10)$$

where  $\mathbf{E}_\Theta = (\mathbf{F}_\Theta^\top \mathbf{F}_\Theta - \mathbf{I})/2$  and  $\mathbf{E}_M = (\mathbf{F}_M^\top \mathbf{F}_M - \mathbf{I})/2 = (\mathbf{C}_M - \mathbf{I})/2$ . Assuming that the material model (*i.e.* the material constants) is independent of temperature, then only  $\mathbf{F}_M$  induces a change in strain energy. If the applied thermal strain is compatible (free expansion), no residual stresses are induced in the mapping from  $\mathbf{B}_\Theta$  to  $\mathbf{B}$ . In this case, the elastic deformation tensor is the identity tensor  $\mathbf{F}_M = \mathbf{I}$  and the corresponding strain energy is zero.

By using the multiplicative decomposition of the deformation gradient tensor and acknowledging that only  $\mathbf{E}_M$  induces a change in strain energy, the second Piola-Kirchhoff (2PK) stress can be written as

$$\mathbf{S} = \frac{\partial \Phi}{\partial \mathbf{E}} = \frac{\partial \Phi}{\partial \mathbf{E}_M} : \frac{\partial \mathbf{E}_M}{\partial \mathbf{E}} = \mathbf{F}_\Theta^{-1} \frac{\partial \Phi}{\partial \mathbf{E}_M} \mathbf{F}_\Theta^{-\top} = \mathbf{F}_\Theta^{-1} \mathbf{S}_M \mathbf{F}_\Theta^{-\top}, \quad (11)$$

which corresponds to a pull-back operation of the 2PK stress from the intermediate configuration  $\mathbf{B}_\Theta$  to the original configuration  $\mathbf{B}_0$ . Similarly, the Lagrangian tangent modulus in the original configuration can be written as:

$$\mathbb{D} = \frac{\partial \mathbf{S}}{\partial \mathbf{E}} = \frac{\partial \mathbf{S}}{\partial \mathbf{E}_M} : \frac{\partial \mathbf{E}_M}{\partial \mathbf{E}}. \quad (12)$$

Using the definition of the elasticity tensor as defined in the intermediate configuration,  $\mathbb{D}_M = \partial \mathbf{S}_M / \partial \mathbf{E}_M$ , the elasticity tensor in the original configuration can be written as:

$$D_{ijkl} = F_{\Theta,ip}^{-1} F_{\Theta,jq}^{-1} F_{\Theta,kr}^{-1} F_{\Theta,ls}^{-1} D_{M,pqrs}, \quad (13)$$

which again corresponds to a pull-back operation of the tangent modulus from the intermediate configuration to the original configuration.

### 1.3 Modelling pre-compression in the substrate using thermal loading

Figure 2(a) presents the procedure to introduce pre-strain in the substrate of the bilayer. Many techniques have been developed to model pre-strain in the substrate using the commercial software ABAQUS, such as developing a user-defined subroutine UMAT [2, 3], and adopting a background mesh technique [4]. In this paper, we introduce the pre-strain using thermal loading. The procedure is shown in Figure 2(b). The initial length of the film and substrate are equal in the FE model. The thermal expansion factor of the film  $\alpha_f$  is set to zero so that it remains strain-free during the thermal loading step (pre-strain process). The thermal expansion factor of the substrate in the  $x$ -direction  $\alpha_{s,x}$  is nonzero but in the  $y$ -direction  $\alpha_{s,y} = 0$ . As shown in Figure 2(b-2), if the substrate is free to expand or shrink, the thermal deformation gradient  $\mathbf{F}_\theta$  in the substrate under temperature variation  $\Delta T$  can be expressed as:

$$\mathbf{F}_\theta = \begin{bmatrix} 1 + \alpha \Delta T & 0 \\ 0 & 1 \end{bmatrix} \quad (14)$$

However, if the horizontal displacements at both ends of the bilayer system are restrained when thermal loading is applied, as shown in Figure 2(b-3), an effective pre-compression is introduced in the substrate and the pre-compression factor can be expressed as:

$$\lambda_{\text{pre}} = \frac{1}{1 + \alpha_s \Delta T}, \quad (15)$$

which is equivalent to the pre-strain procedure shown in Figure 2(a-2). The increase of temperature thus leads to pre-compression in the substrate, and a decrease in temperature to pre-stretch. Due to the zero thermal expansion factor in the film, the film remains stress-free throughout the thermal loading step.

### 1.4 Generalised path-following technique

The linearised equilibrium equation (4) is discretised using 16-noded isoparametric, displacement based, planar finite elements and is implemented in an in-house FE code using MATLAB [5]. Apart from standard arc-length continuation methods, the in-house FE implementation features additional functionality for pinpointing limit and branching points directly, and branch-switching at bifurcation points. In this section, a relatively concise but self-contained outline of this generalised path-following technique is presented. A more detailed exposition can be found in references [5, 6].

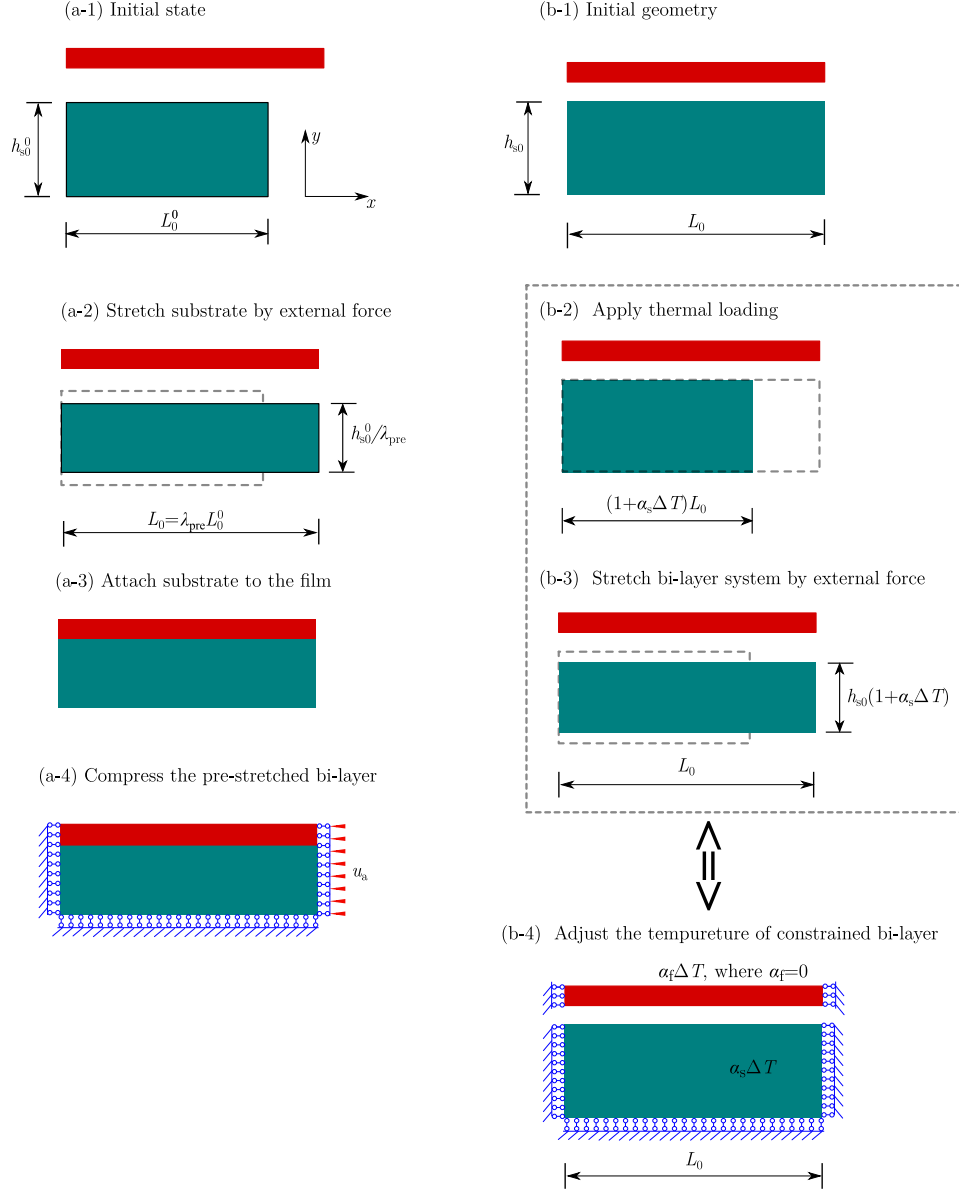


Figure 2: Schematic shows (a) the manufacturing procedure to pre-stretch the bilayer structure and (b) modelling technique adopted to introduce pre-compression in the substrate using thermal loading. Note that the schemes show the procedure to introduce pre-tension. The increase of temperature ( $\Delta T > 0$ ) thus leads to pre-compression in the substrate, and a decrease in temperature ( $\Delta T < 0$ ) to pre-stretch.

### 1.4.1 Path-following of non-critical points

Equilibrium is expressed as a balance between internal and external forces at the finite element nodes. Hence, the force balance of  $n$  equations is written in terms of  $n$  discrete displacement degrees-of-freedom,  $\mathbf{u}$ , and one scalar loading parameter  $\lambda$ ,

$$\mathbf{F}(\mathbf{u}, \lambda) = \mathbf{f}(\mathbf{u}) - \mathbf{p}(\lambda) = \mathbf{0}. \quad (16)$$

By defining an additional scalar arc-length constraint,  $N(\mathbf{u}, \lambda) = \mathbf{n}_u^\top \mathbf{u} + n_\lambda \lambda - \sigma$ , the system of  $n$  equations in  $(n + 1)$  unknowns,  $\mathbf{x} = (\mathbf{u}, \lambda)$ , can be solved:

$$\mathbf{F}^N(\mathbf{x}) = \begin{pmatrix} \mathbf{F}(\mathbf{x}) \\ N(\mathbf{x}) \end{pmatrix} = \mathbf{0}, \quad (17)$$

where  $\mathbf{n}_u$  and  $n_\lambda$  take different forms depending on the nature of the arc-length constraint. Here, Crisfield's cylindrical arc-length constraint [7] is adopted due to its robust performance in the traversal of turning points and snap-back points.

### 1.4.2 Pinpointing singular points

A direct method of pinpointing critical points (singular points of the tangential stiffness matrix) is implemented, which uses a bordering equation to describe the singularity of the tangential stiffness matrix and is then solved using Newton's method. The method is computationally efficient, since the singularity condition forces Newton's method to converge to the singular point directly in a single iterative loading step.

This direct pinpointing procedure is implemented using the so-called nullvector method [8]. The nullvector method is based on the fact that the tangential stiffness matrix,  $\mathbf{F}_{,\mathbf{u}} \equiv \mathbf{K}_T$ , has at least one zero eigenvalue at a singular point, and the associated eigenvector  $\phi$  is in the nullspace of  $\mathbf{K}_T$ . The augmented system is formulated as

$$\mathbf{G}(\mathbf{u}, \lambda, \phi) \equiv \begin{pmatrix} \mathbf{F}(\mathbf{u}, \lambda) \\ \mathbf{K}_T(\mathbf{u}, \lambda)\phi \\ \|\phi\|_2 - 1 \end{pmatrix} = \mathbf{0}. \quad (18)$$

The linearisation of Eq. (18) leads to the iteration matrix for the predictor-corrector solution process

$$\begin{bmatrix} \mathbf{K}_T & \mathbf{F}_{,\lambda} & \mathbf{0} \\ (\mathbf{K}_T\phi)_{,\mathbf{u}} & (\mathbf{K}_T\phi)_{,\lambda} & \mathbf{K}_T \\ \mathbf{0}_{1 \times n} & 0 & \frac{\phi^\top}{\|\phi\|_2} \end{bmatrix} \begin{Bmatrix} \delta\mathbf{u} \\ \delta\lambda \\ \delta\phi \end{Bmatrix} = - \begin{Bmatrix} \mathbf{F}(\mathbf{u}, \lambda) \\ \mathbf{K}_T(\mathbf{u}, \lambda)\phi \\ \|\phi\|_2 - 1 \end{Bmatrix}. \quad (19)$$

The directional derivatives of the tangential stiffness matrix  $\mathbf{K}_T$  and  $\mathbf{F}$  can be approximated using the finite difference method [9]. Equation (19) is solved using a partitioning procedure and the computational cost is similar to that of a standard arc-length continuation step.

In the computer implementation, the 20 smallest magnitude eigenvalues of the tangential stiffness matrix are monitored during continuation along an equilibrium path. When the number of negative eigenvalues between two consecutive converged equilibria changes, a singular point must exist between these two converged equilibria and the pinpointing procedure is triggered. The number of singular points depends on the change in the number of negative eigenvalues,  $N^*$ . The set of eigenvectors  $\Phi$  associated with the smallest  $N^*$  eigenvalues at the last converged equilibrium state,  $(\mathbf{u}^1, \lambda^1)$ , is then extracted. Each  $\phi^j \in \Phi$  for  $j = 1 \dots N^*$  is sequentially seeded to perturb  $(\mathbf{u}^1, \lambda^1)$  as the starting point for the iterative pinpointing procedure. If the solver does not converge, an additional equilibrium point between the previously determined equilibria is determined and the process is repeated.

### 1.4.3 Branch-switching at bifurcations

When a bifurcation point  $(\mathbf{u}^*, \lambda^*)$  is pinpointed, branch-switching to other equilibrium branches is initiated by inserting the nullvector into the displacement field [10]. Therefore, the critical eigenvector at the bifurcation point  $\phi$  is used as a perturbation to the displacement field at the bifurcation point  $\mathbf{u}^*$ :

$$\mathbf{u}^p = \mathbf{u}^* + \xi \frac{\phi}{\|\phi\|_2}, \quad (20)$$

such that the perturbed configuration  $\mathbf{u}^P$  is now used as the predictor for the first step on a new path starting from the bifurcation point. The magnitude of the scaling factor,  $\xi$ , is determined from

$$\xi = \pm \frac{\|\mathbf{u}^*\|_2}{\rho}, \quad (21)$$

where the sign of  $\xi$  controls the direction of path-following along the bifurcated path, and  $\rho$  is a problem-specific constant in the range of 1–100. If  $\rho$  is too small, the algorithm may continue on the primary path; if  $\rho$  is too large, the solution may not converge. Therefore, a restarting facility is embedded into the algorithm such that the magnitude of  $\rho$  can be varied for certain scenarios.

#### 1.4.4 Path-following in two parameters

In preceding subsections, path-following is restricted to a single loading parameter,  $\lambda$ . However, it is often useful and computationally efficient to vary two parameters simultaneously. For instance, in this paper we trace certain equilibria with respect to bilayer length directly rather than conducting expensive parametric studies. To implement this, the equilibrium of internal and external forces, Eq. (16), is adapted to incorporate any number of additional parameters, such that

$$\mathbf{F}(\mathbf{u}, \mathbf{\Lambda}) = \mathbf{f}(\mathbf{u}, \mathbf{\Lambda}_1) - \mathbf{p}(\mathbf{\Lambda}_2) = \mathbf{0}, \quad (22)$$

where  $\mathbf{\Lambda} = [\mathbf{\Lambda}_1^\top \mathbf{\Lambda}_2^\top]^\top = [\lambda_1, \lambda_2, \dots, \lambda_p]^\top$  is a vector that contains  $p$  controlling parameters;  $\mathbf{\Lambda}_1$  corresponds to parameters that influence the internal forces (*i.e.* material properties, geometric dimensions, and temperature) and  $\mathbf{\Lambda}_2$  relates to externally applied mechanical loads, such as forces, moments and tractions.

The expression in Eq. (22) describes  $n$  equilibrium equations in  $n$  displacement degrees of freedom. Because the system is parameterized by  $p$  additional parameters, a  $p$ -dimensional solution manifold in  $\mathbb{R}^{n+p}$  exists. Specific solution subsets on this  $p$ -dimensional manifold can be determined by defining bordering equations,  $\mathbf{g}$ :

$$\mathbf{G}(\mathbf{u}, \mathbf{\Lambda}) \equiv \begin{pmatrix} \mathbf{F}(\mathbf{u}, \mathbf{\Lambda}) \\ \mathbf{g}(\mathbf{u}, \mathbf{\Lambda}) \end{pmatrix} = \mathbf{0}. \quad (23)$$

In total,  $p - 1$  bordering equations are required to define a one-dimensional subset curve on the multi-dimensional solution manifold. For instance, we enforce the criticality condition to solve for a line of critical points, *e.g.*  $\mathbf{g} = \mathbf{F}_{,\mathbf{u}}\phi = \mathbf{0}$  with  $\phi$  a critical eigenvector of the Jacobian  $\mathbf{F}_{,\mathbf{u}}$ . Thus, in the most general form, a vector of  $q$  auxiliary variables,  $\mathbf{v}$ , is added to the bordering equations  $\mathbf{g}$ ,

$$\mathbf{G}(\mathbf{u}, \mathbf{\Lambda}, \mathbf{v}) \equiv \begin{pmatrix} \mathbf{F}(\mathbf{u}, \mathbf{\Lambda}) \\ \mathbf{g}(\mathbf{u}, \mathbf{\Lambda}, \mathbf{v}) \end{pmatrix} = \mathbf{0}. \quad (24)$$

Following the example for critical point tracking referenced above, a critical subset curve in two parameters,  $p = 2$ , is appropriately constrained by the associated bordering equations  $\mathbf{F}_{,\mathbf{u}}\mathbf{v} = \mathbf{0}$  (criticality) and  $\|\mathbf{v}\|_2 = 1$  (normalization constraint). When evaluating a one-dimensional curve, one additional equation is needed to uniquely constrain the system to a solution point  $\mathbf{y} = (\mathbf{u}, \mathbf{\Lambda}, \mathbf{v})$ . Hence,

$$\mathbf{G}^N(\mathbf{y}) \equiv \begin{pmatrix} \mathbf{F}(\mathbf{u}, \mathbf{\Lambda}) \\ \mathbf{g}(\mathbf{u}, \mathbf{\Lambda}, \mathbf{v}) \\ N(\mathbf{u}, \mathbf{\Lambda}) \end{pmatrix} = \mathbf{0}, \quad (25)$$

where  $N$  a scalar equation that plays the role of a multi-dimensional arc-length constraint. A specific solution to Eq. (25) is determined by a consistent linearisation coupled with Newton's method,

$$\mathbf{y}_k^{j+1} = \mathbf{y}_k^j - \left( \mathbf{G}_{,\mathbf{y}}^N(\mathbf{y}_k^j) \right)^{-1} \cdot \mathbf{G}^N(\mathbf{y}_k^j) = \mathbf{y}_k^j + \delta \mathbf{y}_k^j, \quad (26)$$

where the superscript denotes the  $j^{\text{th}}$  equilibrium iteration and the subscript denotes the  $k^{\text{th}}$  load increment. Detailed expressions for tracing loci of critical points (limit and branching points) can be found in Groh *et al.* [5].

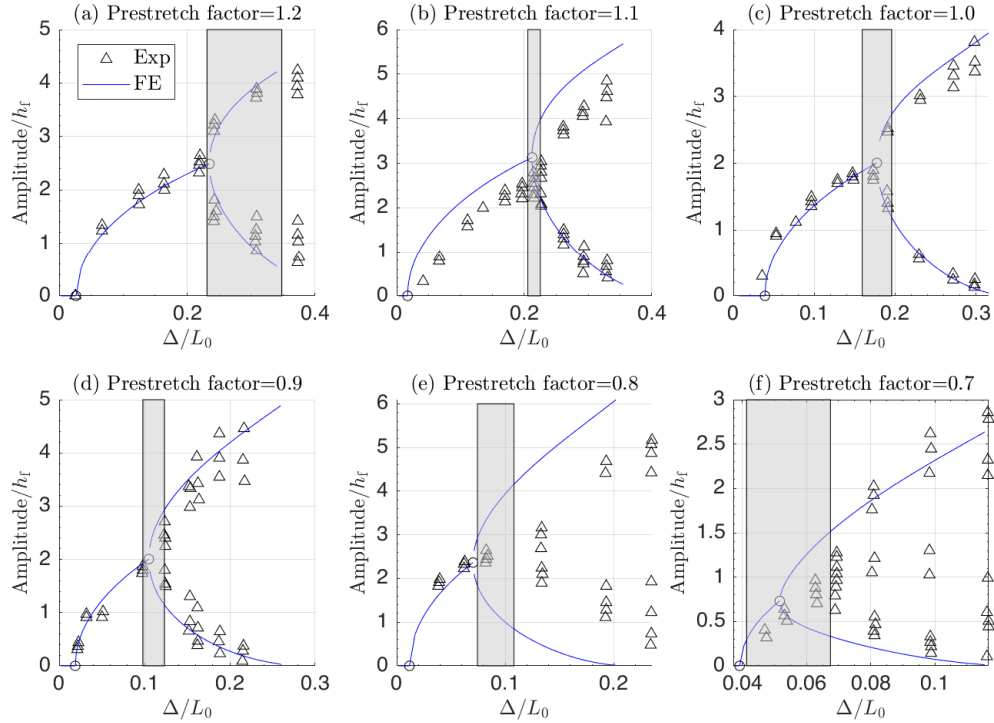


Figure 3: Equilibrium path: normalised wrinkling amplitude *versus* the nominal compression strain of bilayers with different pre-compression/pre-stretch levels. The definition of the wrinkling amplitude can be found in Figure 1(c) of the paper. Blue solid lines and black triangles represent FE simulations and the experimental results, respectively. The nominal modulus ratios between the film and substrate  $E_f/E_s$  are (a) 120, (b) 200, (c) 50, (d) 130, (e) 225 and (f) 35. The details of the experimental set-up and procedure can be found in [2]. Grey shadows represent the range of strains at the secondary bifurcation points from the experiments.

## 1.5 Verification of FE model

Figure 3 presents the comparison of the FE model against the experimental results on bilayers with different pre-compression/pre-stretch levels in the substrate [2]. Note that the film/substrate stiffness ratio and the pre-compression/pre-stretch levels in the substrate are the same as for the specimens in the experiments. The Poisson's ratio in the model is set as 0.43, which yields the best correlation for all cases. Note that preceding studies [11, 12] also reported that adopting a Poisson's ratio between 0.43 and 0.44 in the numerical model leads to the best fit with the experimental results in the wrinkling of bilayers made of PDMS. Note that the length of the FE model is set to twice that of the critical wrinkling wavelength, such that it can accommodate the wrinkling mode progression from sinusoidal wrinkling to period doubling. Moreover, following the modelling strategy in Auguste *et al.* [2], the substrate depth is modelled to be 50 times of the film thickness. The results generally show good correlations with the experimental results.

Figure 4 presents the comparisons of the nominal strains at the secondary bifurcation point, where period doubling occurs, for different pre-compression/pre-stretch levels. The FE model used in this paper can generally correlates well with the experimental results.

## 2 Sensitivity study on the substrate depth of the bilayer

Since there is no consensus on the depth of the substrate required in FE models to approximate the infinite substrate assumption for the post-wrinkling analysis of bilayers, a sensitivity study is conducted to under-

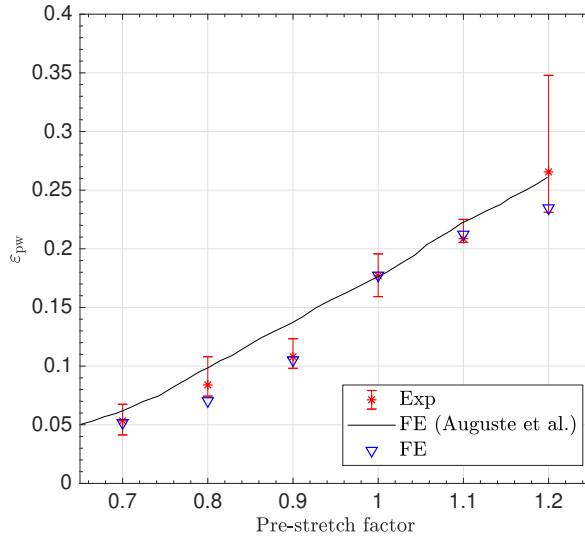


Figure 4: The nominal strain at the secondary bifurcation point, where period doubling occurs, for different substrate pre-compression/pre-stretch levels. The solid black line represents FE results using the incompressible Neo-Hookean model in the commercial FE package ABAQUS. Red stars represent the experimental results, with error bars corresponding to minimal/maximum values for at least 3 samples. The blue triangles represent the FE results using the FE formulation developed in this paper.

stand the effect of the substrate depth on the post-wrinkling behaviour of bilayers. The focus of this section is to determine the substrate depth to satisfy the infinite substrate assumption. A thorough study on the effect of substrate depth on the behaviour of the post-wrinkling behaviour of bilayers is left for future work.

Figure 5 presents the equilibrium path of a bilayer with length  $L_0 = 6L_{crw}$  and substrate depth  $d_s/t_f = 60$ , *i.e.*  $d_s = 12$  mm. The material properties are presented in Table 1. The post-wrinkling behaviour of the bilayer is qualitatively different from the case with ‘infinite’ substrate depth. Even though the critical wrinkling mode is the same as for the infinite substrate and the transition from stable periodic sinusoidal wrinkling to stable period doubling is also observed, the system exhibits qualitatively different behaviour with increasing compression level. Specifically, the final stable wrinkling modes are period tripling and period quadrupling. No further period doubling occurs beyond these basic building blocks. However, when the substrate is infinite, the stable wrinkling mode beyond period doubling is period sextupling and further period doubling occurs when the compression level increases. This difference occurs because the vertical restraint from the bottom edge of the finite substrate stiffens the substrate and prevents the localisation from bumping out to form a period sextupling mode with longer characteristic wavelength.

The depth of substrate to satisfy the infinite-depth assumption depends on the compression level or strain dissipation in the substrate. Therefore, a depth sensitivity study with respect to the post-wrinkling state of interest is required. Using the generalised path-following method [5], we can trace the equilibrium state (including limit and bifurcation points) with respect to a second parameter without having to conduct computationally expensive parametric analyses. This functionality makes it efficient to investigate the effects of substrate depth on the wrinkling behaviour of the bilayer, *i.e.* to determine the threshold value of substrate depth to satisfy the infinity assumption with respect to specific equilibria. We choose the bifurcation point where the basic building blocks with period  $n$ -tupling (quintupling, sextupling, septuple, octupling) becomes unstable and further period doubling occurs as the equilibria of interest. The film/substrate stiffness ratio as well as the thickness of the film are the same as those in the main body of the paper. The pre-compression factor in the substrate is  $\lambda_p = 0.7$ .

Figure 6 presents the depth sensitivity results of the bilayer with respect to varying lengths at the bifurcation point where further period doubling occurs. With the increase of the substrate depth, the nominal critical strain at the bifurcation point decreases, *i.e.* the substrate becomes more compliant due to

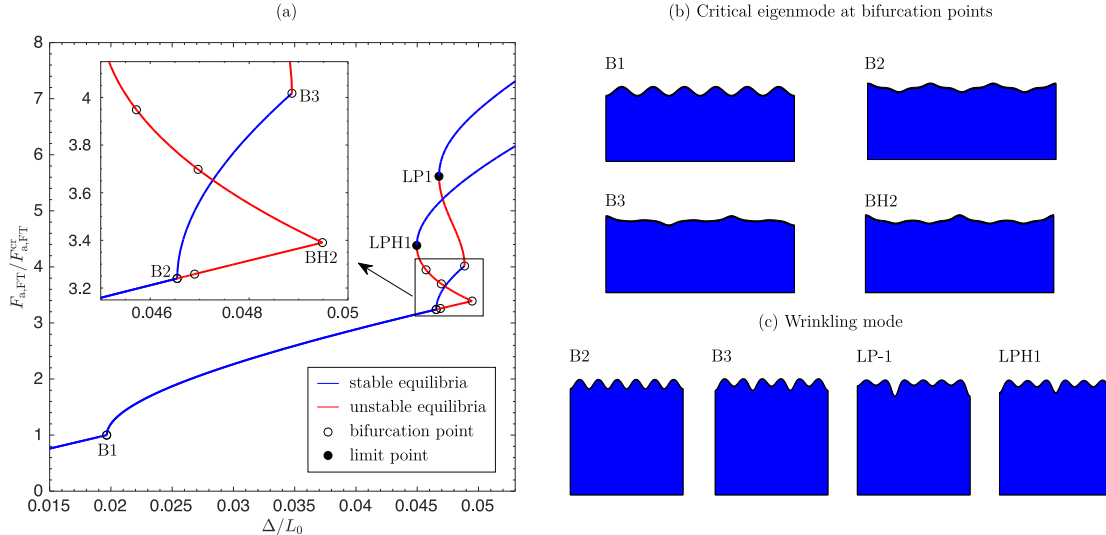


Figure 5: Equilibrium path of a bilayer with length  $L_0 = 6L_{crw}$  and substrate depth  $d_s = 60h_f$ . To aid visualisation, the wrinkling modes have been amplified by a factor of 5. The depth of the substrate does not reflect the actual depth. Note that the full wrinkling stability landscape features significantly more equilibrium paths, and only those paths that lead to the final stable wrinkling mode with a localisation at either or both boundaries are presented here.

reduced restraint from the bottom edge. Beyond the threshold depth, the nominal critical strain remains approximately constant. The Modified Southwell (MS) method [13] is adopted to determine the threshold depth and the results are labelled as red crosses in Figure 6. Beyond the threshold, the substrate can be treated as infinite for the equilibrium state investigated. Note that the threshold increases with the increase in bilayer length or compression level, *i.e.* the nominal compression strain level at the bifurcation point increases with increase in the bilayer length. This implies that the threshold depth to satisfy the infinite depth assumption depends on the compression level.

The depth sensitivity study reveals that the bilayer depth to satisfy the infinity assumption depends on the type of analysis and the state investigated. Generally, the more advanced the post-wrinkling stage investigated, the deeper the substrate required in the FE model. A depth sensitivity study is therefore just as necessary as mesh sensitivity studies in the analysis of wrinkling behaviour in bilayers.

In order to compare the strain energy of bilayers with different lengths, we adopt the same depth for all bilayers with different lengths. We use a substrate depth of  $30L_{crw}$ , which is sufficiently deep to satisfy the infinite substrate assumption.

### 3 Length effects on the critical wrinkling behaviour

Previous work has focused on the wrinkling formation of bilayers with a specific length and suitably applied symmetry conditions at the left and right extremities, where the total length of the system was taken to be an integer multiple of the critical wrinkling wavelength (*i.e.* the wavelength at the transition from the flat to the sinusoidally wrinkled state). Geometric and material imperfections introduced during manufacturing can seed the formation of localisations as compression is increased, and as is shown in this paper, can even divide bilayers into several independent segments of finite length. Therefore, a length sensitivity study of the bilayer system is important to understand the mechanics of the intermediate and deep post-wrinkling behaviour. To introduce the relevant terms used throughout the paper, we first briefly discuss the critical wrinkling behaviour of bilayers with different lengths.

Closed-form solutions exist to predict the compressive strain at which an initially flat bilayer with pre-stretched substrate first wrinkles into a sinusoidal wave of a certain wavelength [4, 14]. These solutions are based on the assumption of incompressible Neo-Hookean solids and do not provide accurate predictions for

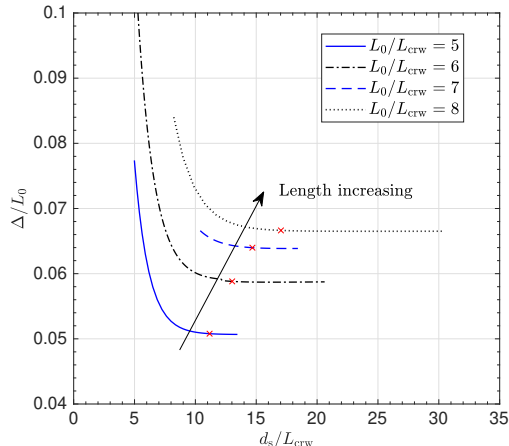


Figure 6: Substrate depth sensitivity results. A multi-parameter continuation of the bifurcation point where the basic stable building blocks become unstable and further period doubling occurs. Red crosses represent the threshold beyond which the nominal compressive strain at the bifurcation point remains constant. This is determined based on the Modified Southwell (MS) method [13].

Table 1: Material and geometric properties of the stiff film/compliant substrate system.

$E_f$ (MPa)	$E_s$ (MPa)	$\nu_f$	$\nu_s$	$h_f$ (mm)	$h_s$ (mm)
1.2	0.01	0.43	0.43	0.2	160

the case of compressibility, particularly when the substrate is significantly pre-compressed. Moreover, these closed-form solutions are independent of bilayer length (assumption of infinite length) and therefore do not describe the variation of critical wrinkling strain with respect to a finite bilayer length. This relationship is, however, important to understand as the ordering and interaction of bifurcations on the fundamental path of the flat and compressed bilayer defines the subsequent wrinkling evolution and therefore the deep post-wrinkling behaviour.

Using the ability to trace critical points through parameter space, we path-follow the locus of the critical wrinkling strain (bifurcation point) with respect to bilayer length. Table 1 presents the geometry and material properties of the film/substrate bilayer system in this length sensitivity study. The parameters chosen are identical to those in Brau *et al.* [11]. The chosen film/substrate thickness ratio satisfies the infinite substrate assumption. The pre-compression level  $\lambda_{\text{pre}}$  in the substrate is set as 0.7, *i.e.*  $\lambda_{\text{pre}} = L_0/L_0^0 = 0.7$ , where  $L_0$  is the length of the film and the substrate after pre-compression;  $L_0^0$  is the initial length of the substrate before pre-compression. For this level of pre-compression, seemingly ‘chaotic’ wrinkling patterns were observed experimentally [2].

Figure 7 presents the relationship between the nominal critical wrinkling strain  $\varepsilon_{\text{crw}}$  (transition from flat to sinusoidally wrinkled) with respect to the bilayer length  $L_0$ . The nominal critical strain is normalised by the critical wrinkling strain of an infinitely long bilayer,  $\varepsilon_{\text{cr,min}}$ , and the bilayer length is normalised by the critical wavelength of the infinitely long bilayer,  $L_{\text{crw}}$ . For the bilayer with properties presented in Table 1, the critical wrinkling wavelength is  $L_{\text{crw}} = 5.34$  mm and the critical strain  $\varepsilon_{\text{cr,min}} = 0.0163$ .

The curves in Figure 7 are determined numerically using the ability of the generalised path-following solver to trace bifurcation points through parameter space. Due to the symmetry boundary conditions at both ends, the bilayer can only accommodate an integer number of half waves. The curves describing the bifurcation point into an integer number of full waves and into a half-integer number of full waves are intertwined, in a manner similar to the critical buckling curves (critical buckling stress *versus* aspect ratio) for axially compressed flat plates [15]. With increasing bilayer length, the nominal critical wrinkling strain approaches  $\varepsilon_{\text{cr,min}}$ . The integer and half-integer curves intersect denoting transitions in the critical wave number (integer to half-integer and *vice versa*) and an interchange between the first and second bifurcation

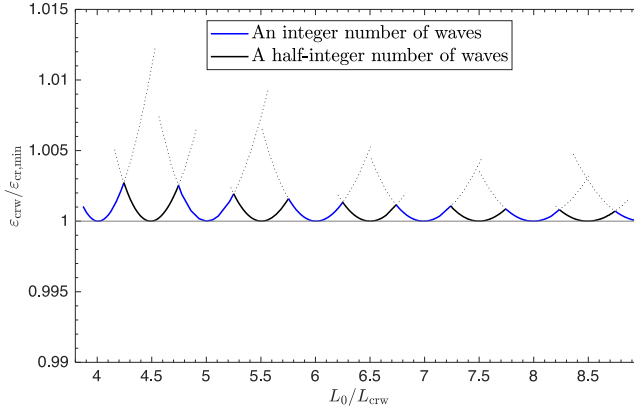


Figure 7: The relationship between the nominal critical wrinkling strain (transition from flat to sinusoidally wrinkled states) and the bilayer length. The solid curves represent the envelope of critical strain; the dotted lines represent the second-order critical wrinkling strain. The geometry and material properties of the bilayer are presented in Table 1; the pre-compression factor in the substrate is  $\lambda_{\text{pre}} = 0.7$ .  $L_0$  and  $L_{\text{crw}}$  are the length of the film (length of the substrate after pre-compression) and the critical wrinkling wavelength of an infinitely long bilayer, respectively.  $\varepsilon_{\text{crw}}$  is the nominal critical wrinkling strain;  $\varepsilon_{\text{cr,min}}$  is the minimal critical wrinkling strain, *i.e.* the critical strain of an infinitely long bilayer.

points on the fundamental path of the flat compressed bilayer. Therefore, the solid envelope curve in Figure 7 describes the onset of wrinkling into the first, critical mode for different bilayer lengths. For bilayer lengths exactly an integer or half-integer multiple of  $L_{\text{crw}}$ , the critical wrinkling strain is equal to that of the infinitely long bilayer, while for intermediate values it is slightly greater. Furthermore, for bilayer lengths exactly an integer or half-integer multiple of  $L_{\text{crw}}$ , the critical wavelength is identical to that of the infinitely long bilayer (*i.e.* equal to  $L_{\text{crw}}$ ), while for intermediate values the number of waves is defined by the nearest integer or half-integer value of  $L_0/L_{\text{crw}}$  with the wavelength appropriately scaled (*i.e.* not equal to  $L_{\text{crw}}$ ). Thus, for non-integer and non-half-integer values of  $L_0/L_{\text{crw}}$ , the mismatch between the energetically favourable wavelength of the infinitely long bilayer and the wavelength permitted by the boundary conditions induces a small increase in the nominal critical strain.

## 4 Length effects on the post-wrinkling behaviour

In this section, we explore the post-wrinkling behaviour of bilayers with integer and non-integer number of full waves and unveil their bifurcation structures using the generalised path-following solver. In particular, we focus on the evolution of the wrinkling pattern from the critical sinusoidal mode into a pattern with pronounced downwards localisations at one or both ends of the bilayer with an upwards hump forming in-between, as a result of sequential period-doubling and symmetry-breaking bifurcations. We find that there is a minimum and a maximum possible distance between two adjacent localisations, *i.e.* a minimum and a maximum possible length to the intermediate hump, and any bilayer system longer than the upper bound ultimately forms an array of smaller ‘building blocks’ that fall within this allowable range.

### 4.1 Cases with integer number of wrinkling waves

#### 4.1.1 $L_0 = 3L_{\text{crw}}$

Figure 8(a) presents the wrinkling landscape of the bilayer with length  $L_0 = 3L_{\text{crw}}$  plotted in terms of engineering strain ( $\Delta/L_0$ ) *versus* the reaction force at the top node of the film normalised by the corresponding reaction force at the onset of wrinkling. The blue segment in the bottom left-hand corner is a stable equilibrium path corresponding to an initially flat state. As compression is increased, this flat state loses stability at a supercritical pitchfork bifurcation (point B1), and upon branch-switching, the bilayer transitions into the critical wrinkling mode showing a sinusoidal wave with three full waves, see Figure 8(c). The sinusoidal

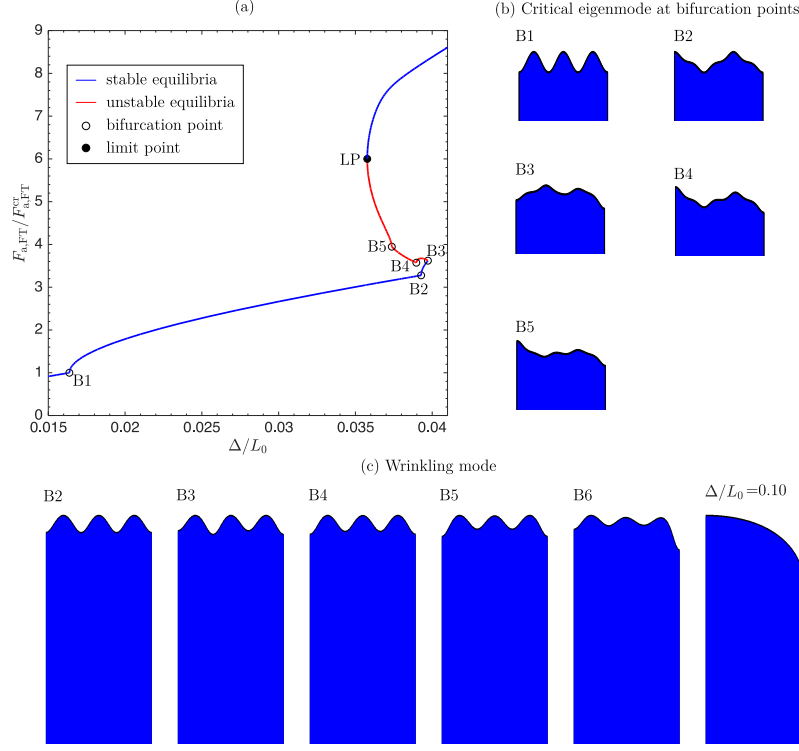


Figure 8: Equilibrium path and wrinkling modes of a bilayer with length  $L_0 = 3L_{crw}$  and pre-compression strain level in the substrate of 0.7. (a) The normalised reaction force at the top node of the film  $F_{a,FT}/F_{a,FT}^{cr}$  versus compressive engineering strain  $\Delta/L_0$ .  $F_{a,FT}^{cr}$  is the force at the top node at the critical wrinkling point B1. (b) Critical eigenmodes at bifurcation points, and (c) the wrinkling mode at critical points. To aid visualisation, the wrinkling modes have been amplified by a factor of 5. The depth of the substrate does not reflect the actual depth. Note that the full wrinkling stability landscape features significantly more equilibrium paths, and only those paths that lead to the final stable wrinkling mode with a localisation at either or both boundaries are presented here.

wrinkling mode is stable until the secondary bifurcation point B2. The critical eigenmode at B2 corresponds to period doubling (see Figure 8(b)), leading to wrinkling modes similar to the case of a bilayer with no pre-strain in the substrate [16]. The period doubling mode then loses stability at bifurcation point B3, which introduces an asymmetric eigenvector into the displacement field (see Figure 8(b)). Branching onto the connected equilibrium path leads to the formation of a localisation at the right end of the bilayer. This equilibrium path is initially unstable and then regains stability at limit point LP1, whence the localisation at the right end is fully formed and the bilayer forms an elongated hump corresponding to period sextupling, as shown in Figure 8(c) at  $\Delta/L_0 = 0.1$ . The equilibrium path remains stable until a crease occurs at the right end, *i.e.* the bilayer has bulged sufficiently to form contact with material on the right side of the applied symmetry plane.

Note that the symmetry boundary condition at the left end inhibits symmetry breaking of the elongated hump mode. Hence, in longer bilayers, *e.g.* a bilayer of twice the length  $L_0 = 6L_{crw}$ , the period sextupling mode observed for  $L_0 = 3L_{crw}$  may regain stability at a different critical point.

#### 4.1.2 $L_0 = 4L_{crw}$

The equilibrium path of the bilayer with  $L_0 = 4L_{crw}$  is presented in Figure 9. There are four full waves in the critical eigenmode at the critical bifurcation point B1. Similar to the previous case with  $L_0 = 3L_{crw}$ , the critical eigenmode at bifurcation point B2 corresponds to period doubling and branch-switching leads to a

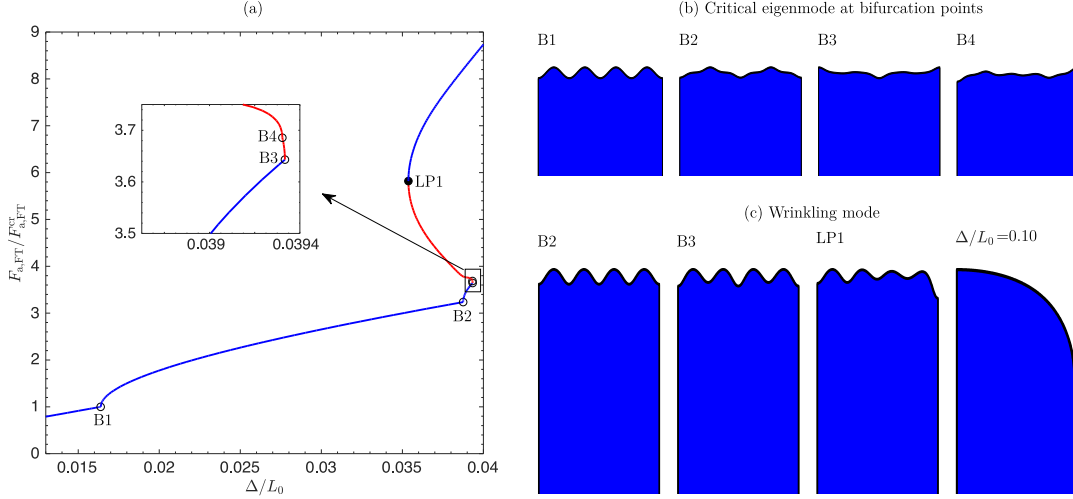


Figure 9: Equilibrium path and wrinkling modes of a bilayer with length  $L_0 = 4L_{crw}$  and pre-compression strain in the substrate of 0.7. The details are the same as described in Figure 8.

stable period doubling mode on the tertiary path. Hence, period doubling is a stable wrinkling mode in the initial post-wrinkling compression range.

The period doubling mode then loses stability beyond bifurcation point B3, with the critical eigenmode being symmetric about the mid-span but anti-symmetric about each quarter-span. Branch-switching at B3 leads to the formation of unstable period quadrupling. As shown in the inset of Figure 9(a), there is a bifurcation point B4 with an anti-symmetric critical eigenmode immediately after branch-switching from B3. The connected path at B4 leads to the formation of a localisation at one end of the bilayer. The system then regains stability at limit point LP1, from which period octupling is a stable mode. The final stable wrinkling mode before the formation of a crease (self-contact across a symmetry line) is an elongated hump with a localisation at one end, see the wrinkling mode at  $\Delta/L_0 = 0.1$  in Figure 9(c). Similar to the case with  $L_0 = 3L_{crw}$ , the stability of this period octupling mode requires further analysis when the symmetry boundary condition at the left end is relaxed, *i.e.* an analysis for a bilayer with  $L_0 = 8L_{crw}$ .

#### 4.1.3 $L_0 = 5L_{crw}$

Figure 10 presents the bifurcation landscape of the bilayer with  $L_0 = 5L_{crw}$ . The critical wrinkling mode accommodates five full waves. Before B3, the wrinkling mode progression essentially follows the same pattern as in the preceding two cases, *i.e.* from sinusoidal wrinkling to period doubling modes. Period doubling then loses stability beyond bifurcation point B3. The profile of the corresponding asymmetric eigenmode is similar to a combination of the eigenmodes of the bilayers with  $L_0 = 3L_{crw}$  and  $L_0 = 4L_{crw}$  at B3, see Figures 8(b) and 9(b), respectively. Branch-switching at B3 leads to an unstable equilibrium path and the formation of a localisation at the right end of the bilayer. Stability is then restored and lost again at limit points LP1 and LP2, respectively. In displacement-controlled end-compression, the bilayer jumps from B3 to an equilibrium state between LP1 and LP2 directly, where the wrinkling pattern is irregular, see LP1 and LP2 in Figure 10(c).

Path-following further, the wrinkling mode restores left-right symmetry at the pitchfork bifurcation B4 by forming a period quintupling mode, as shown in Figure 10(c). Note that stable period quintupling was previously observed numerically in bilayers with pre-compressed substrates [3]. Unlike the preceding two cases ( $L_0 = 3L_{crw}$  and  $L_0 = 4L_{crw}$ ), there exists an independent stable period quintupling mode over a relatively large range of compressive strains, *i.e.*  $\Delta/L_0 = 0.0353$  to  $\Delta/L_0 = 0.051$  between B4 and B5. Further period doubling is triggered at the bifurcation point B5 with the addition of an anti-symmetric critical eigenmode leading to a mode with ten-fold periodicity (decoupling). Further loading leads to the formation of a crease at the right end of the domain at the nominal compressive strain of  $\Delta/L_0 = 0.1057$ .

This is the first example where the bilayer has formed a single outwards hump delimited by two inwards

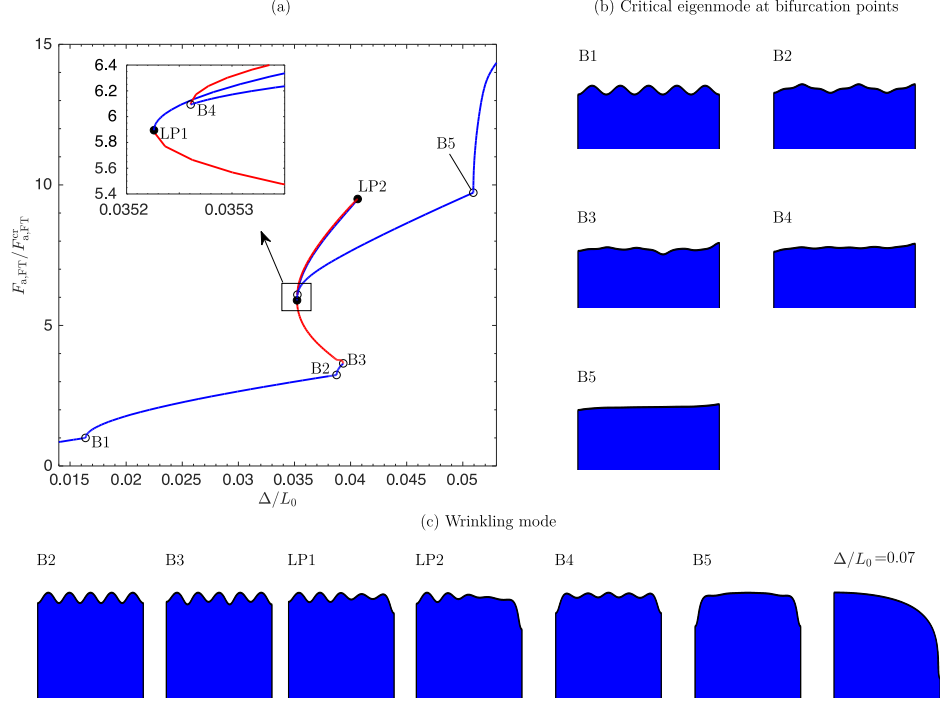


Figure 10: Equilibrium path and wrinkling modes of a bilayer with length  $L_0 = 5L_{crw}$  and pre-compression strain in the substrate of 0.7. The details are the same as described in Figure 8.

localisations at either end (see period quintupling at B5 in Figure 10(c)) and a further doubled mode delimited by one localisation at the right end only (see period decoupling at  $\Delta/L_0 = 0.07$  in Figure 10(c)). This demonstrates the bilayers tendency to sequentially lengthen the wrinkling wavelength as the applied compressive strain is increased. The initial sinusoidal mode first bifurcates into period doubling by preserving symmetry and then bifurcates into period quintupling by breaking and restoring symmetry. The intermediate compressive strain range is therefore governed by a stable period quintupling mode (an outward hump) bounded by two localisations. In the deep post-wrinkling range the wrinkling wavelength lengthens again through additional doubling to form period decoupling. For a system of length  $L_0 = 10L_{crw}$  this would correspond to two adjacent period quintupling blocks merging into one larger period decoupling block. The period quintupling mode is therefore a ‘building block’ that governs the bilayer’s behaviour in the intermediate strain range.

Also note that the transition from period doubling to period quintupling is accompanied by a sequence of snap-back and snap-through instabilities as well as breaking of symmetry groups, leading to an irregular pattern of the wrinkling mode. This irregularity may explain the seemingly ‘chaotic’ or irregular wrinkling modes observed in experiments. Hence, irregular patterns arise as a result of symmetry-breaking at bifurcations, and specifically as transition paths between two symmetric regular patterns.

#### 4.1.4 $L_0 = 6L_{crw}$

Figure 11 presents the equilibrium path, critical eigenmodes and wrinkling modes at selected equilibria along the manifold for  $L_0 = 6L_{crw}$ . The bifurcation structure and the wrinkling progression on the primary and secondary paths are essentially identical to those in the preceding three cases. On the tertiary path, the profile of the critical eigenmodes of the first and second bifurcation points (labelled B3 and BH4) are similar to the critical eigenmodes of the first bifurcation point on the tertiary path for  $L_0 = 4L_{crw}$  and  $L_0 = 3L_{crw}$ , respectively. Specifically, the critical eigenmode for B3 is anti-symmetric, while it is symmetric for BH4. Branch-switching from both B3 and BH4 leads to period sextupling. Period sextupling is thus another ‘building block’ that governs the bilayer’s behaviour in the intermediate strain range.

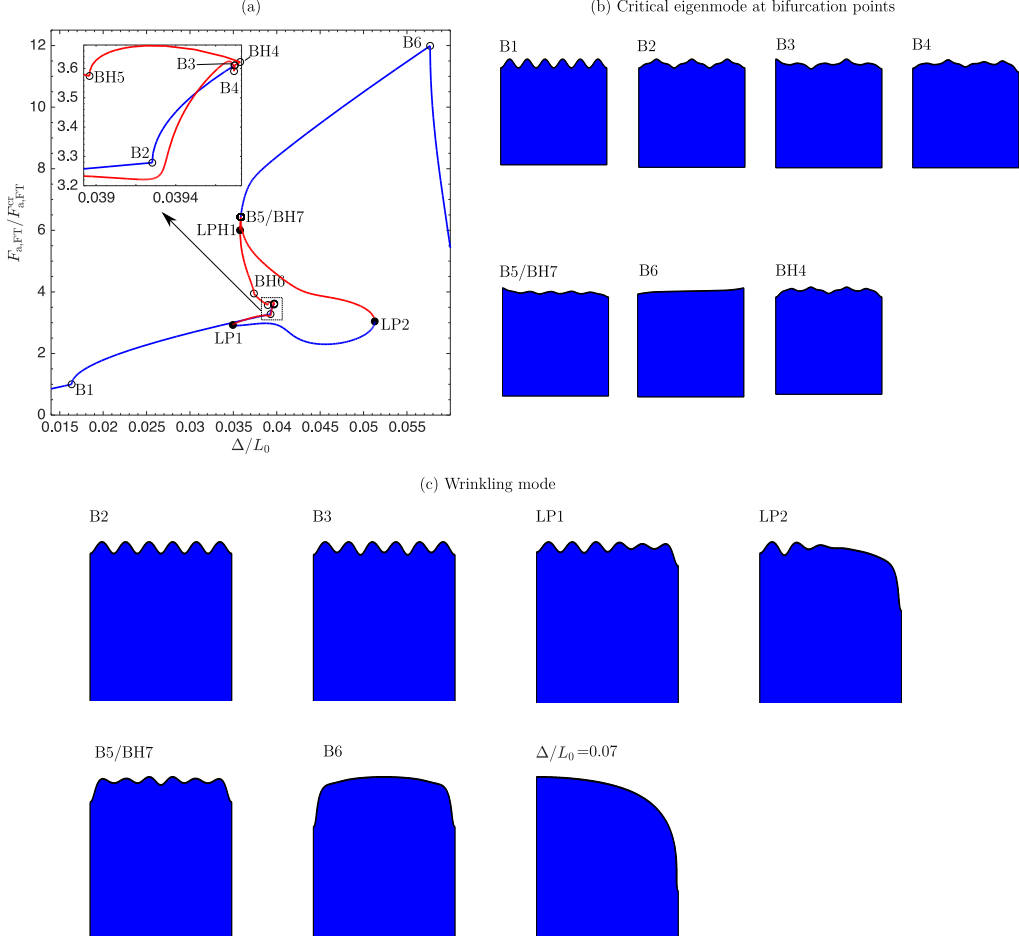


Figure 11: Equilibrium path and wrinkling modes of a bilayer with length  $L_0 = 6L_{\text{crw}}$  and pre-compression strain in the substrate of 0.7. The details are the same as described in Figure 8.

The two bifurcated paths from B3 and BH4 connect at the bifurcation point B5/BH5. On the path branching from B3, the wrinkling mode follows a transition that initially breaks and then restores symmetry, leading to a stable irregular wrinkling pattern between limit points LP1 and LP2, as is observed in the case for  $L_0 = 5L_{\text{crw}}$ . For the path branching from BH4, symmetry is always preserved during the transition process and the equilibrium path is essentially identical to the bilayer with half the length, *i.e.*  $L_0 = 3L_{\text{crw}}$ . The system with  $L_0 = 6L_{\text{crw}}$  is of course equivalent to two  $L_0 = 3L_{\text{crw}}$  systems end-to-end but with no symmetry condition at the mid-span. Owing to the release of this symmetry condition at the mid-span, the bilayer of length  $L_0 = 6L_{\text{crw}}$  regains stability at bifurcation point BH5 and not at LPH1 as was previously observed for  $L_0 = 3L_{\text{crw}}$  in Figure 8 (denoted limit point LP1 for  $L_0 = 3L_{\text{crw}}$ ).

With further loading into the advanced strain regime, the stable period sextupling from the intermediate strain regime loses stability at bifurcation point B6. As was observed for the period quintupling-to-decoupling transition for  $L_0 = 5L_{\text{crw}}$ , an additional doubling occurs on the associated bifurcated path from B6 to form period duodecupling (twelve-fold periodicity). A crease with self-contact across the symmetry line occurs at the nominal compression strain of  $\Delta/L_0 = 0.0915$ .

#### 4.1.5 $L_0 = 7L_{\text{crw}}$

The bifurcation landscape with the associated critical eigenmodes at critical points and selected wrinkling modes is presented in Figure 12 for bilayer length  $L_0 = 7L_{\text{crw}}$ . The progression of the wrinkling mode from sinusoidal wrinkling to period doubling is the same as for the preceding cases. For conciseness and

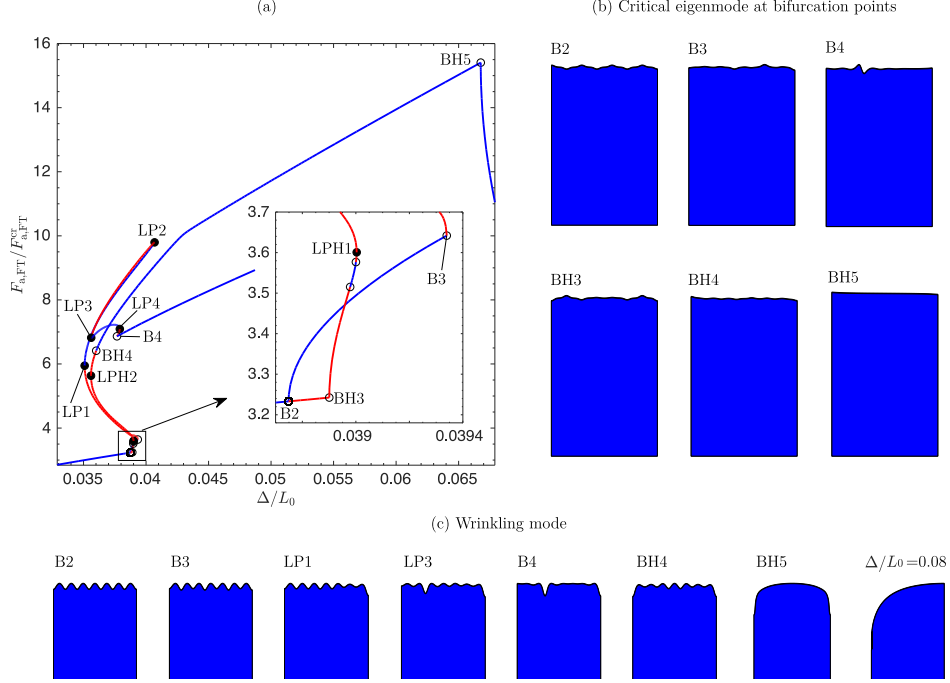


Figure 12: Equilibrium path and wrinkling modes of a bilayer with length  $L_0 = 7L_{\text{crw}}$  and pre-compression strain in the substrate of 0.7. The details are the same as described in Figure 8. The path bifurcating from BH3 leads to period septupling, which is separated from the stable secondary path by unstable equilibrium segment B2–BH3. Under monotonically increasing end-shortening, the bilayer follows the path B2–B3 instead, which leads to period quintupling.

clarity, the fundamental path as well as the first bifurcation point are not presented in Figure 12. Unlike the preceding cases for which a single and unique stable ‘building block’ existed in the intermediate strain range, for the case of  $L_0 = 7L_{\text{crw}}$  there exist two regular patterns delimited by localisations: period quintupling (see B4 in Figure 12(c)) and period septupling (see BH4 in Figure 12(c)). The co-existence of different stable wrinkling modes was previously posited as an explanation for the ‘chaotic’ behaviour observed in experiments of bilayers with pre-compressed substrates [2] in that different stable wrinkling modes with similar total potential energy ‘compete’ and the occurrence of either pattern along a long bilayer is driven by starting conditions.

Period quintupling is on the path bifurcating from point B3, which is the point where period doubling loses stability. The critical eigenmode of the bifurcation point is very similar to a combination of the corresponding critical eigenmodes for  $L_0 = 3L_{\text{crw}}$  and  $L_0 = 4L_{\text{crw}}$ , see B3 in Figure 8(b) and B3 in Figure 9(b). There are sequential snap-backs and snap-throughs along the bifurcated path, corresponding to the formation of localisations at the right end of the bilayer and at the left one-third span, see *e.g.* point LP3 in Figure 12(c). The full periodicity of the wrinkling pattern, *i.e.* period quintupling, is restored at bifurcation point B4. Also note that bifurcation point B4 connects to the secondary path that bifurcates from the second bifurcation point on the fundamental path (flat bilayer) with 7.5 waves in the critical eigenmode.

The period septupling mode is unattainable via a standard loading history of monotonically increasing end-compression because the regions of stable period septupling are separated by interstitial unstable equilibria. This may provide a possible reason why the period septupling mode is not reported or observed in experiments. Specifically, branch-switching from bifurcation point BH4 does not connect back with any fundamental, secondary or tertiary paths as observed in the preceding two cases for  $L_0 = 5L_{\text{crw}}$  and  $L_0 = 6L_{\text{crw}}$ . Instead, the period septupling equilibrium path connects to the bifurcation point where fourteen-fold periodicity (quattuordecupling) is fully formed, *i.e.* a half hump with no additional wrinkling in the film, which is the stable wrinkling mode in the advanced strain regime.

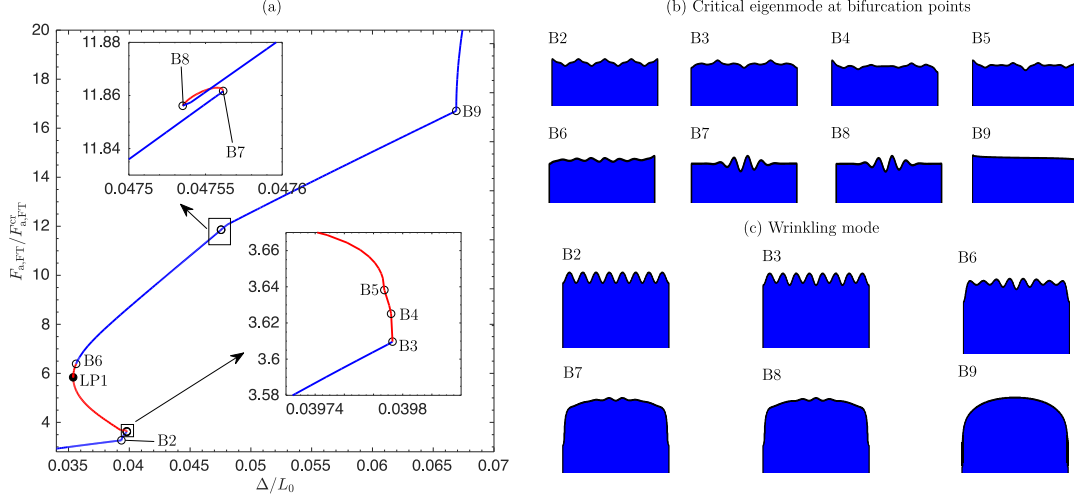


Figure 13: Equilibrium path and wrinkling modes of a bilayer with length  $L_0 = 8L_{\text{crw}}$  and pre-compression strain in the substrate of 0.7. The details are the same as described in Figure 8.

#### 4.1.6 $L_0 = 8L_{\text{crw}}$

In the preceding case with  $L_0 = 7L_{\text{crw}}$ , it was demonstrated that the bilayer can accommodate different stable wrinkling patterns, *i.e.* period quintupling and period septupling. The multiplicity of stable wrinkling modes and complexity of the associated equilibrium manifold increases further as the bilayer lengthens. Therefore, the time required to explore all possible equilibrium branches and identify all stable wrinkling modes increases considerably. For this reason, we now focus only on the stable wrinkling modes featuring a single hump and localisations at both ends using so-called ‘homotopy’ continuation. The known period septupling mode for the case of  $L_0 = 7L_{\text{crw}}$  is chosen as a starting point and the length of the bilayer is then smoothly increased to identify the equivalent octupling mode for a length of  $L_0 = 8L_{\text{crw}}$  (and nonupling mode for  $L_0 = 9L_{\text{crw}}$  in the next section). Once the stable octupling mode with a single hump is obtained, we have identified a starting point to trace the entire equilibrium path.

Figure 13 presents the equilibrium path of the bilayer with  $L_0 = 8L_{\text{crw}}$ . The stable ‘building block’ in the intermediate strain range featuring a localisation at either end of the bilayer is a period octupling wrinkling mode. The bifurcation structure of the bilayer is similar to the preceding cases, where stable period octupling starts from a bifurcation point with anti-symmetric critical eigenmode (B6). Further period doubling then occurs at bifurcation point B9 to form a wrinkling pattern with stable 16-fold periodicity (sexdecupling), which then governs the advanced strain range.

Compared to the case with half the length, *i.e.*  $L_0 = 4L_{\text{crw}}$ , the bifurcation structure is more complex as a result of releasing the symmetry boundary condition at the mid-span. Additional bifurcation points with anti-symmetric critical eigenmodes arise, *i.e.* B4, B6, B7, and B8. In particular, the existence of B4 prevents the bilayer from restoring stability at limit point LP1 as was previously observed for  $L_0 = 4L_{\text{crw}}$  (point LP1 in Figure 9). Moreover, the pair of additional bifurcation points (B7 and B8) on the stable period octupling path correspond to snap-back and snap-through instabilities accompanying symmetry breaking and symmetry restoring with respect to the mid-span, with the number of full waves in the wrinkling mode changing from 8 to 7 and the valley in the wrinkling mode at mid-span transitioning into a peak, see B7 and B8 in Figure 13(c). Moreover, similar to the case with  $L_0 = 7L_{\text{crw}}$ , the bilayer can also accommodate period quintupling modes (one full and one half hump as shown for point B4 in Figure 12(c)), which initially bifurcates from the secondary bifurcation point on the fundamental path featuring 7.5 sinusoidal waves in the critical eigenmode. For brevity, this quintupling mode is not shown in Figure 13.

Similar to the septupling mode for  $L_0 = 7L_{\text{crw}}$ , the stable octupling mode for  $L_0 = 8L_{\text{crw}}$  is also separated from the natural loading path by interstitial unstable equilibria. Moreover, there are no stable segments directly connected to B3 or B4. The bilayer will thus undergo a dynamic transition upon reaching B3 and will either stabilise in the mode with least total potential or the closest local minimum potential. In this case, the

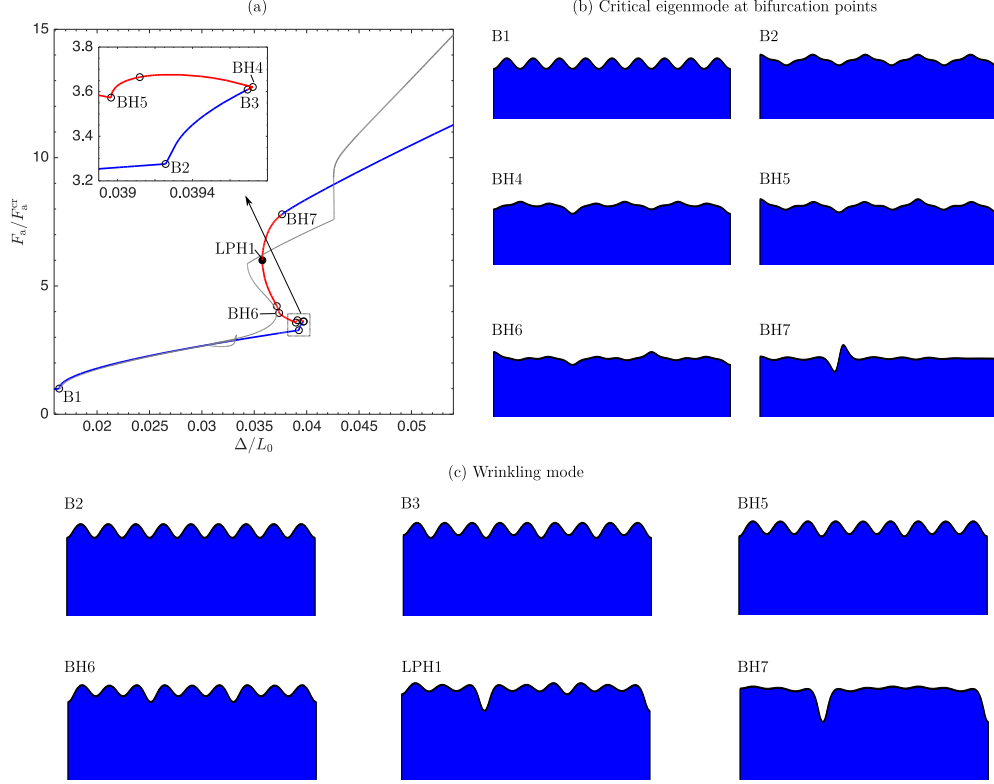


Figure 14: Equilibrium path and wrinkling modes of a bilayer with length  $L_0 = 9L_{crw}$  and pre-compression strain in the substrate of 0.7. The details are the same as described in Figure 8. The grey curve represents the equilibrium path leading to period octupling, which has been presented in the paper. Note that the bifurcation structure in the dashed rectangle is essentially the same as presented in Figure 11.

two possible modes are period octupling (global minimum) or period quintupling (local minimum). A dynamic analysis is required to determine the stabilised wrinkling pattern. Note also that branch-switching from the bifurcation point B6 does not connect back to any bifurcation point on fundamental/secondary/tertiary paths throughout a standard loading history of monotonically increasing end-compression.

#### 4.1.7 $L_0 = 9L_{crw}$

Figure 14 presents the equilibrium path as well as the wrinkling modes and critical eigenmodes at selected equilibria for the bilayer with  $L_0 = 9L_{crw}$ . Grey curves represent the path leading to period octupling, which has been discussed in details in the paper. Coloured curves here represent the equilibrium path branch-switching from B1, which leads to a stable wrinkling mode with 9 sinusoidal waves and then evolves into stable period sextupling (one full and one half hump bounded by localisations) in the intermediate strain level. Note that the bifurcation diagram of the equilibrium path is essentially identical to the case with  $L_0 = 6L_{crw}$ .

#### 4.1.8 Summary and n-tupling building blocks

From the numerical results discussed in this subsection that investigated the bifurcation structure beyond the initial sinusoidal post-wrinkling regime, a set of stable period n-tupling modes was identified that are characterised by the formation of inward localisations at either end of the wrinkling pattern. These n-tupling modes are period quintupling, period sextupling, period septupling, and period octupling and were denoted as stable ‘building blocks’ that govern the intermediate strain range. With further loading beyond the intermediate post-wrinkling regime and into the advanced strain range, these regular wrinkling patterns

undergo further period doubling that leads to the formation of a single outward hump until eventually a crease forms through self-contact across imposed symmetry lines. The significance of these ‘building blocks’ is that bilayers longer than  $L_0 = 9L_{\text{crw}}$  form a combination of these stable n-tupling wrinkling modes in the intermediate strain range.

## 4.2 Cases with non-integer waves

In the preceding subsection, we explored the bifurcation structure of bilayers with overall length equal to an integer number of the critical wrinkling wavelength. In practice, the length of bilayers is rarely exactly an integer multiple of the critical wavelength. Moreover, the symmetry boundary conditions adopted at both ends of the bilayer also accommodate half waves. Therefore, it is important to understand the wrinkling behaviour of bilayer lengths equal to a non-integer number of the critical wavelength.

Here, two bilayers with  $L_0 = 4.455L_{\text{crw}}$  and  $L_0 = 4.720L_{\text{crw}}$  are selected. These chosen lengths are immediately to the left and right of the minimum at  $L_0 = 4.5L_{\text{crw}}$  on the buckling curve in Figure 7. The critical eigenmodes of these two bilayers corresponding to the first bifurcation point on the fundamental path are the same, featuring 4.5 sinusoidal waves, whereas the second eigenmodes corresponding to the second bifurcation point on the fundamental path are different.

Figure 15 presents the equilibrium path of the bilayer with  $L_0 = 4.455L_{\text{crw}}$ . The first two bifurcation points on the fundamental equilibrium path of the flat bilayer feature 4.5 and 4 sinusoidal waves, see B1 and BH2, respectively in Figure 15. Branch-switching from the first (critical) bifurcation point B1 leads to a stable periodic wrinkling mode with 4.5 waves; however, further branch-switching along the ensuing equilibrium path does not lead to stable periodic wrinkling patterns.

Branch-switching from the second bifurcation point on the fundamental path (BH2) initially leads to an unstable equilibrium path with 4 periodic sinusoidal waves, but the periodic wrinkling mode stabilises at the bifurcation point BH3. With further loading, period doubling occurs at the bifurcation point BH4, reflecting the scenario observed for  $L_0 = 4L_{\text{crw}}$ . However, the sequential bifurcation structure is different from the case with  $L_0 = 4L_{\text{crw}}$ . Specifically, the critical eigenmode at the bifurcation point BH5 is anti-symmetric. Branch-switching from this bifurcation point leads to sequential snap-back and snap-through instabilities, see LPH1 and LPH2 in Figure 15(c), with associated irregular wrinkling patterns. The symmetry of the wrinkling mode is restored at the bifurcation point BH6, where stable period quadrupling is formed and this is here identified as another stable ‘building block’ in the intermediate strain range. As observed for the bilayers in the previous subsection, further loading into the advanced strain regime then causes further period doubling, leading to a half hump with a localisation at one end. The entire bifurcation structure is essentially identical to that in the case with  $L_0 = 9L_{\text{crw}}$  in Figure 14. However, due to the additional symmetry boundary condition, some symmetry-breaking bifurcation points vanish.

Figure 16(a) presents the equilibrium path of the bilayer with  $L_0 = 4.720L_{\text{crw}}$ . In this case, the first two bifurcations on the fundamental equilibrium path of the flat bilayer feature 4.5 and 5 waves in the critical eigenmodes, see B1 and BH2 in Figure 16(b), respectively. Branch-switching from B1 leads to a stable periodic sinusoidal wrinkling mode with 4.5 waves but further loading does not lead to a stable period quadrupling or period quintupling mode. Similar to the preceding case with  $L_0 = 4.455L_{\text{crw}}$ , there are isolated stable equilibria on the path bifurcating from the secondary bifurcation point BH2. However, unlike the preceding case with  $L_0 = 4.455L_{\text{crw}}$  and the case with integer number of full waves, stable period doubling is not observed on the tertiary path branch from the bifurcation point BH4. Instead, there is a bifurcation point BH5 on the tertiary path immediately after branch-switching, with the critical eigenmode being anti-symmetric. Branch-switching from bifurcation point BH5 leads to sequential snap-back and snap-through instabilities and finally a restoration of a symmetric wrinkling mode at bifurcation point BH6. The symmetry breaking and restoring process to form stable period quintupling is similar to the case with  $L_0 = 5L_{\text{crw}}$  in Figure 10. Once stable period quintupling has formed across the intermediate strain range, further period doubling into a period decoupling mode (ten-fold periodicity) occurs in the advanced strain range, as was observed in the case for  $L_0 = 5L_{\text{crw}}$ .

Note that the two paths for  $L_0 = 4.455L_{\text{crw}}$  and  $L_0 = 4.72L_{\text{crw}}$  that lead to period quadrupling and period quintupling modes, respectively, both bifurcate from the secondary bifurcation point on the fundamental path and are separated from the stable fundamental path by unstable equilibrium segments. Therefore, these states are not expected to arise smoothly under monotonically increasing loading from the unloaded

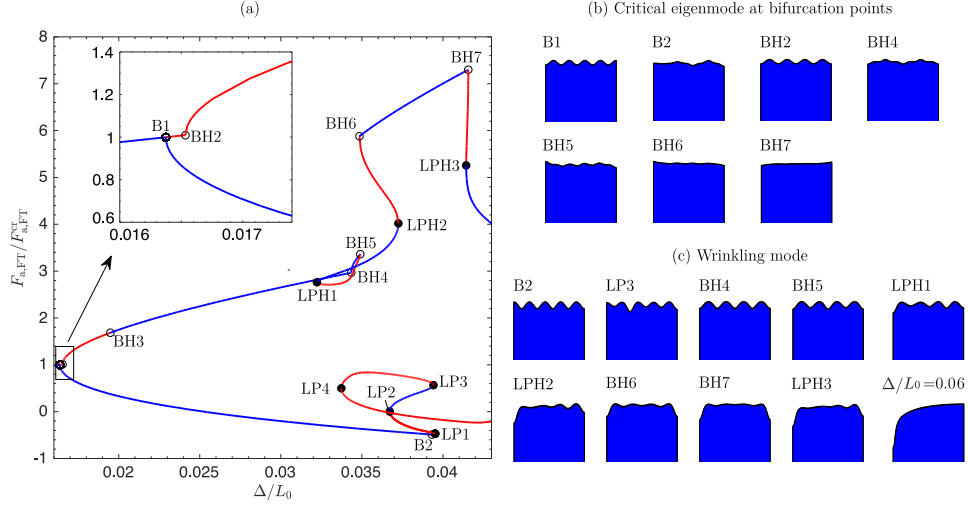


Figure 15: Equilibrium path and wrinkling modes of a bilayer with length  $L_0 = 4.455L_{crw}$  and pre-compression strain in the substrate of 0.7. The details are the same as described in Figure 8. The path leading to period quadrupling bifurcates from the second bifurcation point on the fundamental path BH2. Under natural loading (monotonically increasing end-shortening), the bilayer bifurcates at B1 and follows the secondary path B1–B2.

state. In the presence of certain imperfections, for instance, the inclusion of dents at both ends of the bilayer, the bilayer may favour a bespoke response that leads to stable period quadrupling or quintupling from the unloaded state. One of the most efficient techniques to tailor the response of nonlinear structures by embedding certain geometric perturbation in the perfect geometry is called ‘modal nudging’ [17].

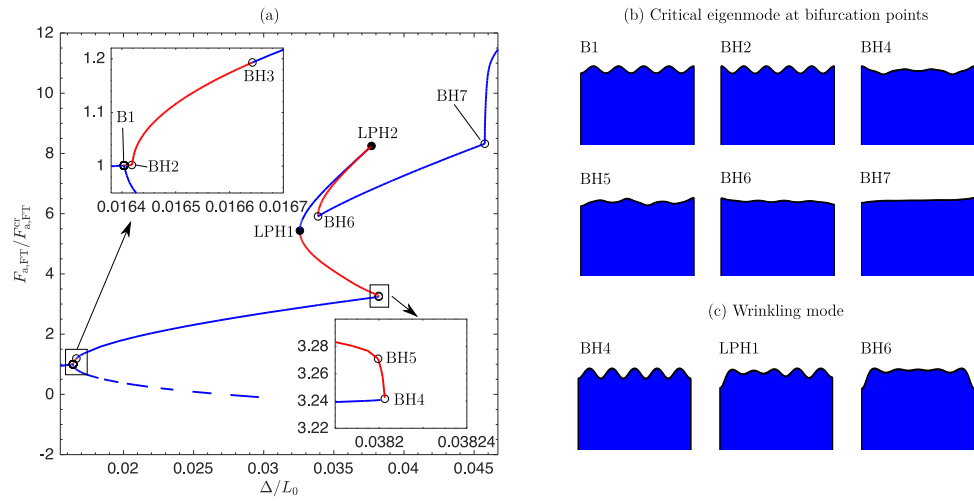


Figure 16: Equilibrium path and wrinkling modes of a bilayer with length  $L_0 = 4.72L_{crw}$  and pre-compression strain in the substrate of 0.7. The details are the same as described in Figure 8. The path leading to period quintupling bifurcates from BH2. The equilibria between B1–BH2 are unstable. Hence, under natural loading (monotonically increasing end-shortening), the bilayer bifurcates at B1 and follows the stable secondary path with 4.5 sinusoidal wrinkling waves (see the dashed blue curves).

## References

- [1] J. Bonet, A. J. Gil, R. D. Wood, *Nonlinear solid mechanics for finite element analysis: statics*, Cambridge University Press, 2016.
- [2] A. Auguste, L. Jin, Z. Suo, R. C. Hayward, The role of substrate pre-stretch in post-wrinkling bifurcations, *Soft Matter* 10 (34) (2014) 6520–6529.
- [3] J. Liu, K. Bertoldi, Bloch wave approach for the analysis of sequential bifurcations in bilayer structures, *Proceedings of the Royal Society A: Mathematical, Physical and Engineering Sciences* 471 (2182) (2015) 20150493.
- [4] Y. Cao, J. W. Hutchinson, Wrinkling phenomena in Neo-Hookean film/substrate bilayers, *Journal of Applied Mechanics* 79 (3), 031019 (04 2012).
- [5] R. Groh, D. Avitabile, A. Pirrera, Generalised path-following for well-behaved nonlinear structures, *Comput. Meth. Appl. Mech. Eng.* 331 (2018) 394–426.
- [6] A. Eriksson, Structural instability analyses based on generalised path-following, *Computer Methods in Applied Mechanics and Engineering* 156 (1998) 45–74.
- [7] M. A. Crisfield, A fast incremental/iterative solution procedure that handles snap-through, *Computers and Structures* 13 (1-3) (1981).
- [8] G. Moore, A. Spence, The calculation of turning points of nonlinear equations, *SIAM Journal on Numerical Analysis* 17 (4) (1980) 567–576.
- [9] P. Wriggers, J. C. Simo, A general procedure for the direct computation of turning and bifurcation points, *International Journal for Numerical Methods in Engineering* 30 (1) (1990) 155–176.
- [10] W. Wagner, P. Wriggers, A simple method for the calculation of postcritical branches, *Engineering Computations* 5 (1988) 103–109.
- [11] F. Brau, H. Vandeparre, A. Sabbah, C. Poulard, A. Boudaoud, P. Damman, Multiple-length-scale elastic instability mimics parametric resonance of nonlinear oscillators, *Nature Physics* 7 (1) (2011) 56–60.
- [12] L. Zhuo, Y. Zhang, The mode-coupling of a stiff film/compliant substrate system in the post-buckling range, *International Journal of Solids and Structures* 53 (2015) 28–37.
- [13] J. Shen, M. A. Wadee, Local–global mode interaction in thin-walled inelastic rectangular hollow section struts part 2: Assessment of existing design guidance and new recommendations, *Thin-Walled Structures* 145 (2019) 106184.
- [14] J.-Y. Sun, S. Xia, M.-W. Moon, K. H. Oh, K.-S. Kim, Folding wrinkles of a thin stiff layer on a soft substrate, *Proceedings of the Royal Society A: Mathematical, Physical and Engineering Sciences* 468 (2140) (2012) 932–953.
- [15] S. P. Timoshenko, S. Woinowsky-Krieger, *Theory of plates and shells*, McGraw-hill, 1959.
- [16] F. Brau, P. Damman, H. Diamant, T. A. Witten, Wrinkle to fold transition: influence of the substrate response, *Soft Matter* 9 (34) (2013) 8177–8186.
- [17] B. Cox, R. Groh, D. Avitabile, A. Pirrera, Modal nudging in nonlinear elasticity: Tailoring the elastic post-buckling behaviour of engineering structures, *Journal of the Mechanics and Physics of Solids* 116 (2018) 135–149.